Journal of Materials Chemistry A

ROYAL SOCIETY OF CHEMISTRY

PAPER

View Article Online
View Journal | View Issue

Check for updates

Cite this: J. Mater. Chem. A, 2024, 12, 11563

Oxygen vacancy-induced efficient hydrogen spillover in $Ni_{17}W_3/WO_{3-x}/MoO_{3-x}$ for a superior pH-universal hydrogen evolution reaction†

Yiqing Sun,[ab] Yiwei Bao,[ab] Di Yin,[c] Xiuming Bu,*[b] Yuxuan Zhang,[c] Kaihang Yue,[b] Xiaoshuang Qi,[b] Ziyan Cai,[b] Yongqiang Li,[d] Xiulan Hu,*[a] Johnny C. Ho*[ce] and Xianying Wang*[b]

Received 31st January 2024
Accepted 28th March 2024

DOI: 10.1039/d4ta00729h

rsc.li/materials-a

Searching for a stable and efficient electrocatalyst for the hydrogen evolution reaction is still challenging, especially under a wider pH operation condition. In this study, a multicomponent $Ni_{17}W_3/MoO_{3-x}/WO_{3-x}$ catalyst was designed and synthesized, in which the unique hierarchical structure of entangled nanorods confined in a polyhedral framework ensures the maximum utilization of active sites. Significantly, electrochemical performance can be regulated by adjusting the oxygen vacancy concentration of the metal support. Combined with various characterization techniques, we discovered that abundant oxygen vacancies in the MoO_{3-x}/WO_{3-x} support not only significantly enhanced the hydrogen insertion/extraction kinetics in the metal oxide but also increased the hydration capacity, resulting in an efficient hydrogen adsorption/transfer/desorption kinetics on the $Ni_{17}W_3/MoO_{3-x}/WO_{3-x}$ surface and interface. As a result, the fabricated electrocatalyst exhibits an ultralow overpotential of 16, 42, and 14 mV at 10 mA cm^{-2} in alkaline, neutral, and acid electrolytes, respectively. Our work proves the important role of metal oxide supports in the hydrogen spillover process.

Introduction

Water electrolysis systems driven *via* renewable energy sources to produce hydrogen offer a potential solution to the dual challenges of energy crisis and environmental pollution.[1–5] For the hydrogen evolution reaction (HER), in the half-reaction of water electrolysis, platinum is the best-performing catalyst owing to its optimized free energy of hydrogen bonding (ΔG_H).[6–9] However, its high cost makes it difficult to achieve large-scale applications. Furthermore, the catalyst inevitably experiences localized proton concentration changes during the reaction process; therefore, a well-qualified catalyst should be able to adapt to a wide pH range of operating environments to make device operation more stable and reliable.

The construction of metal/metal oxides has been proven to be an efficient strategy since a metal oxide support modulates an active metal phase's hydrogen intermediate (H*) adsorption/desorption behavior through strong metal–support interactions (SMSIs).[10–12] Among various metal oxide support candidates, WO_x has attracted widespread attention because of its excellent electronic conductivity and outstanding synergistic effect with active metals.[13] Meanwhile, the hydrogen spillover phenomenon is observed on the metal/WO_x interface in two steps. First, H* transfers from the metal ($\Delta G_{H\text{-metal}} < 0$) to the WO_x surface ($\Delta G_{H\text{-support}} > 0$),[14] causing the active metal surface to rapidly re-expose. Then, H* inserts/extracts into the WO_x lattice to provide additional active sites for the hydrogenation of WO_x. Previous studies have primarily focused on reducing the hydrogen spillover transfer barrier through active metal modification (EG–Pt/CoP and Pt SA/WO_x).[15,16] To the best of our knowledge, few studies have investigated the effect of support modification strategy on the HER performance.

In this work, we designed and synthesized $Ni_{17}W_3/MoO_{3-x}/WO_{3-x}$ multicomponent catalysts *via* an *in situ* confinement method, in which $Ni_{17}W_3$ functions as the active metal phase and MoO_{3-x}/WO_{3-x} serves as the support. Moreover, the fabricated catalyst's oxygen vacancy concentration can be adjusted simply by changing the mole ratio between MoO_3 and WO_3. Next, by tracking phase evolution and mass/charge transfer

[a]College of Materials Science and Engineering, Nanjing Tech University, Puzhu South Road No. 30, 211816, Nanjing, Jiangsu, China. E-mail: whoxiulan@163.com
[b]CAS Key Laboratory of Materials for Energy Conversion, Shanghai Institute of Ceramics, Chinese Academy of Sciences, Shanghai 200050, P. R. China. E-mail: buxiuming@mail.sic.ac.cn; wangxianying@mail.sic.ac.cn
[c]Department of Materials Science and Engineering, City University of Hong Kong, Kowloon, Hong Kong SAR 999077, P. R. China. E-mail: johnnyho@cityu.edu.hk
[d]Joint Laboratory of Graphene Materials and Applications, Shanghai Institute of Microsystem and Information Technology, Chinese Academy of Science, Shanghai 200050, P. R. China
[e]Institute for Materials Chemistry and Engineering, Kyushu University, Fukuoka 816-8580, Japan

† Electronic supplementary information (ESI) available. See DOI: https://doi.org/10.1039/d4ta00729h

kinetics with *in situ* Raman and *in situ* electrochemical impedance spectroscopy techniques, the superior performance of the catalyst results from the abundant oxygen vacancies of the metal oxide support, which accelerates phase transition from the metal oxide to hydrogen bronze, further resulting in a rapid H* adsorption/transfer/desorption kinetics on the $Ni_{17}W_3/MoO_{3-x}/WO_{3-x}$ surface and interface. As a result, the fabricated $Ni_{17}W_3/MoO_{3-x}/WO_{3-x}$ catalyst shows superior HER performance at all pH values, requiring only 14, 42, and 16 mV overpotential to reach a geometric current density of 10 mA cm^{-2} in acid, neutral, and alkaline electrolytes, respectively. Our research confirms the practical potential of $Ni_{17}W_3/MoO_{3-x}/WO_{3-x}$ and provides new design concepts for metal/metal oxide catalysts.

Experimental

Preparation of NW_1M_1R

Carbon cloth (CC) with an area of 1 × 1 cm^2 was first immersed in nitric acid for surface treatment. Then, the treated carbon cloth was ultrasonically cleaned with ethanol and DI consecutively for 20 minutes to remove surface impurities before synthesis. 0.68 mmol $Ni(NO_3)_2 \cdot 6H_2O$, 0.0625 mmol $(NH_4)_{10}H_2(W_2O_7)_6 \cdot xH_2O$ and 0.15 mmol $(NH_4)_6Mo_7O_{24} \cdot 4H_2O$ were dispersed in 16 mL DI water and then heated to 60 °C for 1 h to obtain a uniform solution. Next, the solution was poured into a 25 mL Teflon-lined stainless autoclave with the CC immersed in it, followed by heating at 150 °C for 18 h. After hydrothermal treatment, Mo–$Ni_4W_6O_{21}$ was washed with water and methanol and dried at 60 °C for 6 h. Finally, it was annealed under an Ar/H_2 (5 v% H_2) atmosphere in a tube furnace at 500 °C for 2 h. The obtained sample was labelled as NW_1M_1R. The product without the Mo-doped process was named NWP, while the product without the W-doped process was named NMR.

Physical characterization

The microstructures of the catalysts, as well as the corresponding elemental distributions, were derived by SEM, TEM, HRTEM, and EDS mapping on FESEM, Quanta FEG 450 and FEI, TECNAI F20. The phase structure of each catalyst was characterized by X-ray diffraction at a scan rate of 5° min^{-1} and a 2θ range of 10–80°. The chemical composition and electronic structure of the catalysts were analyzed by X-ray photoelectron spectroscopy. Oxygen vacancy concentration was determined by electron paramagnetic resonance (EPR, EMXnano, Bruker, USA).

Electrochemical measurement

The CV and LSV polarization curves were tested using an electrochemical workstation (GAMRY) with a standard three-electrode system. The prepared catalyst was used as the working electrode, Ag/AgCl as the reference electrode, and the carbon rod as the counter electrode. Moreover, the polarization curves were corrected by *iR* compensation (85%). Each catalyst's bilayer capacitance (C_{dl}) was tested by CV polarization curves in 1.0 M KOH electrolyte at different scan rates (20–100 mV s^{-1}) in the voltage range of 0.173–0.273 V *vs.* RHE. *In situ* electrochemical impedance spectra were obtained in the 0 to −0.065 V voltage range *vs.* RHE. All HER stability tests were performed without *iR* compensation.

In situ electrochemical Raman measurement

In situ Raman tests were performed on a LabRAM HR 800 using a custom-made Raman electrolytic cell with NW_1M_1R and NWP as the working electrodes, Ag/AgCl as the reference electrode, and Pt as the counter electrode, respectively. In this case, the individual potentials (−0.05 V to −0.60 V) were controlled by an electrochemical workstation, and the Raman signals were collected at 70 s intervals at each potential. All tests were performed without *iR* compensation.

Anion exchange membrane water electrolysis (AEMWE) performance

The AEMWE performance was evaluated by testing the CV polarization curves in 1.0 M KOH electrolyte using NW_1M_1R as the cathode and platinum-modified NiFe LDH as the anode over a voltage range of 1.0 to 2.0 V (5 mV s^{-1}). The stability test was conducted using chronopotentiometry at 1 A cm^{-2} for 90 hours at room temperature. The performance and stability tests were performed with no *iR* compensation.

Theoretical calculation

The adsorption energy calculated by spin-polarized density-functional theory (DFT) was computed using the Vienna *Ab initio* Simulation Package (VASP) and the Perdew–Burke–Ernzerhof functional within generalized gradient approximation. During the calculation process, the electronic iterations convergence was 10^{-5} eV, and Hellmann–Feynman forces were 0.02 eV $Å^{-1}$. Surface isolation was performed using a 10 Å vacuum plate. The *k*-points mesh was set into 4 × 3 × 1 for structural optimization, and the corresponding vacuum layer was 20 Å.

Results and discussion

The $Ni_{17}W_3/MoO_{3-x}/WO_{3-x}$ ternary heterostructure was synthesized *via* the *in situ* confinement method with the $Ni_4W_6O_{21}$ polyhedron as the soft template. As shown in Fig. 1a, the precursors were first prepared *via* a hydrothermal method, followed by heat treatment in a mixed Ar/H_2 atmosphere to obtain the final product (the detailed preparation process is shown in the Experimental section). It should be noted that MoO_3 was selected to modify the support because MoO_3 and WO_3 are similar; both can transfer to bronzes upon H insertion.[17] Interestingly, when the precursor contains only $Ni(NO_3)_2$ and $(NH_4)_{10}H_2(W_2O_7)_6$, typical micrometer-sized particles with polyhedral morphology were fabricated (denoted as NWP). After introducing $(NH_4)_6Mo_7O_{24}$, twisted and intertwined nanorods were confined for *in situ* nucleation growth in the polyhedral framework (denoted as $NW_1M_{0.5}R$, NW_1M_1R and $NW_1M_{1.5}R$ when the molar ratio W and Mo in the precursor is 1 : 0.5, 1 : 1 and 1 : 1.5). The scanning electron microscopy (SEM) images

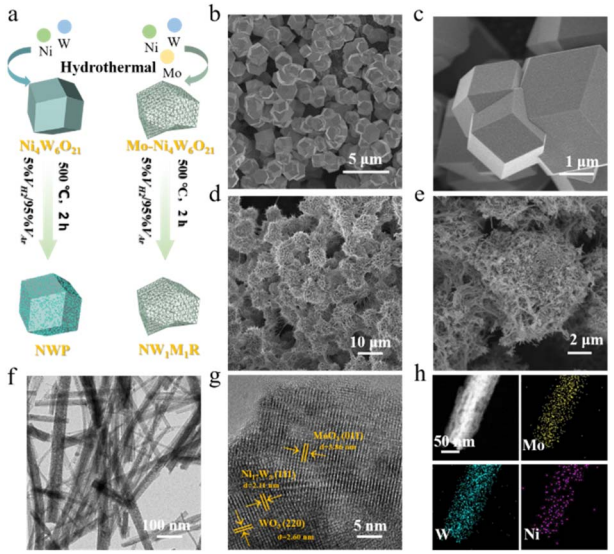

Fig. 1 (a) Schematic illustration of the synthesis of NWP and NW_1M_1R. (b and c) SEM images of NWP. (d and e) SEM images of NW_1M_1R. (f) TEM and (g) HRTEM images of NW_1M_1R. (h) EDS mapping of NW_1M_1R for Mo, W, and Ni elements.

exhibit a precise morphology observation for the electrocatalyst. Regular particles with a size of ≈3 μm were obtained when only Ni and W elements were in the precursor, and tiny nanoparticles were randomly attached to the microparticle surface (Fig. 1b, c and S1†). Compared with $Ni_4W_6O_{21}$ precursors that have not been annealed at high temperatures, the surface is smooth, and no nanoparticles are formed, indicating that the formation of these nanoparticles is due to the phase separation (Fig. S2†). Then, after Mo introduction, the NWMR catalyst maintains a polyhedral shape but is assembled from tangled nanorods (Fig. 1d, e and S3†). However, the NMR catalyst without adding W shows nanorod morphology (Fig. S4†). Based on the transmission electron microscopy (TEM) image, the diameter of the nanorods is about 45 nm (Fig. 1f). The above characterization results suggest that the introduction of Mo successfully induced a morphological transition, with a significant increase in the surface area from 33.524 $m^2\ g^{-1}$ to 53.52 $m^2\ g^{-1}$ (Fig. S5†), which is conducive to the total exposure of the active stable sites in the electrolyte.

Further detailed structural information is explored by high-resolution TEM (HRTEM). The characteristic lattice fringes of 0.211, 0.260, and 0.386 nm correspond well to the (111) plane of $Ni_{17}W_3$, (220) plane of WO_3 and (011) plane of MoO_3, respectively (Fig. 1g). In addition, the characteristic lattice fringes of 0.210, 0.260, and 0.340 nm in NWP catalysts correspond to the (111) plane of $Ni_{17}W_3$, (220) plane of WO_3, and (−110) plane of WO_2, respectively (Fig. S6†).

Combined with the crystal and phase information obtained through the X-ray diffraction (XRD) patterns (Fig. S7–S9†), the characteristic peaks of NWP located at 23.48°, 33.60°, 41.40° and 48.04° correspond to the (020), (202), (222) and (040) facets of WO_3 (JCPDS 46-1096), and the peaks at 25.79° and 37.07° are indexed to the (011) and (−211) planes of WO_2 (JCPDS 05-0431).[18] Also, three peaks at 43.70°, 50.88°, and 74.82° correspond to the diffraction of (111), (200) and (220) planes of the $Ni_{17}W_3$ phase, respectively (JCPDS 65-4828).[19] Thus, the crystal phase composition for NWP is $Ni_{17}W_3/WO_2/WO_3$. On the other hand, for the $NW_1M_{0.5}R$, NW_1M_1R, and $NW_1M_{1.5}R$ samples, the characteristic peaks for WO_2 disappear totally, and new peaks located at 23.05°, 25.30°, 36.09°, and 47.28° appear, which can be assigned to MoO_3 (JCPDS 89-1554).[20] Thus, the crystal phase composition for these three samples is $Ni_{17}W_3/MoO_3/WO_3$. The characteristic NMR peak at 50.9° corresponds to the (310) plane of Ni_4Mo (JCPDS 03-1036). The energy dispersive X-ray (EDX) elemental mapping of NW_1M_1R (Fig. 1h) shows that Mo, Ni, and W are present and evenly distributed throughout the entire nanorod, indicating the successful preparation of $Ni_{17}W_3/MoO_3/WO_3$ ternary heterostructures.

The surface chemical composition and electronic structure of the obtained electrocatalysts are then assessed by X-ray photoelectron spectroscopy (XPS). Obviously, the obtained spectrum confirms the existence of Ni, Mo, W, and O in $NW_1M_{0.5}R$, NW_1M_1R, $NW_1M_{1.5}R$ (Fig. S10†). The high-resolution Ni 2p spectrum in Fig. S11† shows two peaks at ∼852.8 and ∼869.2 eV attributed to metallic state Ni^0, while the other four peaks are corresponding to Ni^{2+} (∼856.1 and ∼873.7 eV) and Ni^{3+} (∼857.6 and ∼875 eV) and their corresponding satellite peaks (∼861.7 and ∼880.1 eV).[21] The high-resolution W 4f spectrum (Fig. S12†) of NW_1M_1R displays three doublets, which can be attributed to W^0 (∼31.4 and ∼33.6 eV), W^{4+} (∼32.8 and ∼33.9 eV) and W^{6+} (∼35.5 and ∼37.5 eV), respectively.[22,23] In addition, the Mo 3d spectrum (Fig. S13†) exhibits three sets of peaks, corresponding to Mo^{4+} (∼229.4 and ∼231.7 eV), Mo^{5+} (∼230.6 and ∼234.3 eV) and Mo^{6+} (∼232.7 and ∼235.5 eV), respectively.[24,25] It is also noted that after Mo introduction, the Ni 2p and W 4f binding energies of NW_1M_1R are the largest compared with the NWP, blue-shifted by 0.3 and 0.6 eV. For the Mo 3d spectrum, no obvious binding energy shift is observed.[26,27] Moreover, the O 1s XPS spectrum shows three typical peaks centered at 530.4, 531.5, and 532.6 eV, corresponding to the lattice oxygen, oxygen vacancy, and absorbed oxygen, and NW_1M_1R shows the highest oxygen vacancy concentrations (Fig. S14†).[28,29] To further confirm the presence of oxygen vacancies, the prepared catalysts were subjected to electron paramagnetic resonance (EPR) spectroscopy. $NW_1M_{0.5}R$, NW_1M_1R and $NW_1M_{1.5}R$ all show EPR signals at $g = 2.002$, while NWP shows a signal at $g = 2.003$.[30,31] The EPR results further support that NW_1M_1R exhibits a stronger EPR signal than $NW_1M_{0.5}R$, $NW_1M_{1.5}R$ and NWP (Fig. S15†). When the W and Mo atomic ratio is 1 : 1, the sample exhibits the highest oxygen vacancy concentration, which can be attributed to the lattice mismatch between cubic phase α-WO_3 and monoclinic phase β-MoO_3. The above electronic structure analysis results indicate that the optimized metal oxide ratio can not only adjust the oxygen vacancy concentration but also enhance the interface contact among these material phases.[32]

To shed light on the excellent electrochemical performance of the fabricated electrocatalyst, we first investigated the HER activity of each catalyst in 1.0 M KOH *via* linear scanning voltammetry (LSV). As shown in Fig. 2a and S14,† among all the

tested samples, NW_1M_1R establishes the best HER catalytic performance, needing a lowest overpotential of only 16 mV to achieve the current density of 10 mA cm^{-2}, which is significantly superior than those of NWP (72 mV), $NW_1M_{1.5}R$ (44 mV), $NW_1M_{0.5}R$ (54 mV), NMR (51 mV) and Pt/C (29 mV), respectively. Then, the corresponding Tafel slope of NW_1M_1R is fitted to 34.9 mV dec^{-1}, superior to those of NWP (72.4 mV dec^{-1}), $NW_1M_{1.5}R$ (54.8 mV dec^{-1}), $NW_1M_{0.5}R$ (62 mV dec^{-1}), NMR (54.1 mV dec^{-1}) and commercial Pt/C (49.2 mV dec^{-1}) (Fig. 2b and S16†), indicating a fast HER kinetics.[33] Specifically, the Tafel slope value of NW_1M_1R is close to 30 mV dec^{-1}, suggesting that the HER process follows the Volmer–Tafel mechanism, where hydrogen is formed by the combination of neighboring adsorbed H* rather than by the combination of H* and water molecules in the electrolyte. In addition, electrochemical impedance spectroscopy (EIS) was further employed to analyze the HER kinetics at the interface between the electrode and electrolyte (Fig. 2d). The Nyquist plots show that NW_1M_1R has the smallest radius, while the equivalent circuit diagram (Fig. S17†) yields that NW_1M_1R also has the lowest charge transfer resistance (R_{ct} = 2.8 Ω). Notably, compared to the recently reported HER catalysts, the excellent HER performance of NW_1M_1R is almost the best among them (Fig. 2c and Table S1†).

After that, double-layered capacitances (C_{dl}) are measured by cyclic voltammetry (CV) at different sweep rates from 20 to 100 mV s^{-1} to assess the electrochemical active surface area (ECSA) of each catalyst (Fig. S18 and S19†). It is observed that the C_{dl} value of NW_1M_1R is 22.24 mF cm^{-2}, which is 4.82 times higher than that of NWP (4.61 mF cm^{-2}). When the current densities are normalized with respect to ECSA, NW_1M_1R still exhibits a much larger current density than other samples during the entire voltage range, indicating that NW_1M_1R is indeed intrinsically more active than NWP, $NW_1M_{1.5}R$, and $NW_1M_{0.5}R$ (Fig. S20†). In addition to the high catalytic performance demonstrated, the Faraday efficiency of the NW_1M_1R was determined to be 99.37%, nearly 100% (Fig. S21†). The long-term HER performance of NW_1M_1R at different current densities and 40 hours for each current density (160 hours in total) and at a high current density of 500 mA cm^{-2} (100 hours) shows that the voltage has no apparent upward trend (Fig. 2e and S22†), indicating that this unique hierarchical structure improves the stability by preventing aggregation, which is usually one of the main factors leading to catalyst deactivation. The almost unchanged NW_1M_1R nanostructure, even after 160 h of stability testing, further supports the superiority of the hierarchical structure during the HER process (Fig. S23 and S24†). After long-term stability, the sample was also subjected to XPS characterization (Fig. S25–S27†). The comparison of the pre- and post-reaction states showed that Ni, Mo, and W promote the HER process in the form of high valence states. In addition, because of the superior HER performance under alkaline conditions, an AEM flow cell is assembled with the NW_1M_1R electrocatalyst, which serves as a cathode, and the homemade NiFe LDH serves as the anode (Fig. S28†). The polarization curves of the AEM are shown in Fig. 2f; commercial Pt/C is added for comparison. Notably, the NiFe LDH (+)||NW_1M_1R (−) couple achieves a current density as high as 1 A cm^{-2} at 2 V, which is superior to that of the commercial NiFe LDH (+)||Pt/C (−) and most of the reported electrocatalyst (Fig. S29†). More importantly, the stability of the assembled AEM flow cell is investigated at a constant current density of 1 A cm^{-2}, which exhibits excellent durability for 90 hours, indicating the NW_1M_1R electrode to be a promising HER electrocatalyst in the AEM water electrolyzer (Fig. 2g).

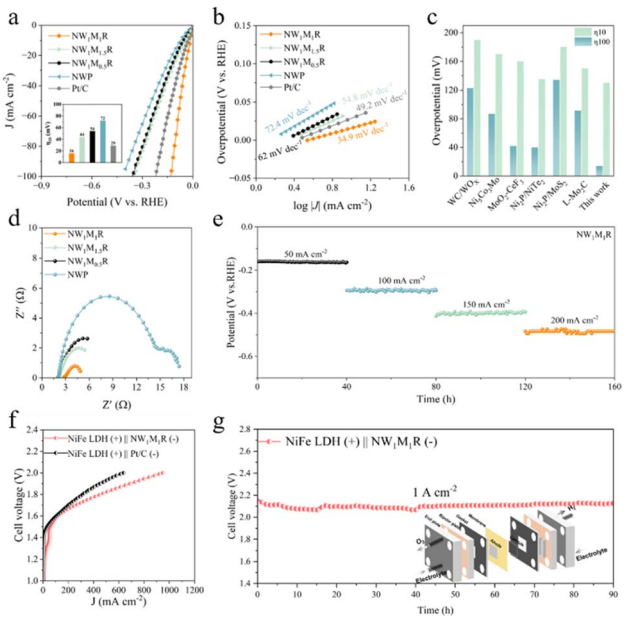

Fig. 2 (a) LSV curves of NW_1M_1R, $NW_1M_{1.5}R$, $NW_1M_{0.5}R$, NWP, and Pt/C (inset: overpotentials at 10 mA cm^{-2} for these electrocatalysts) in 1.0 M KOH. (b) Tafel slope of different electrodes. (c) HER performance comparison of recently reported electrocatalysts. (d) Nyquist plots of NW_1M_1R, $NW_1M_{1.5}R$, $NW_1M_{0.5}R$ and NWP. (e) Multistep chronopotentiometry curves of NW_1M_1R at 50, 100, 150, and 200 mA cm^{-2} for 160 h (without *iR* correction). (f) Polarization curves of the NiFe LDH (+)||NW_1M_1R (−) and NiFe LDH (+)||Pt/C (−) in the AEM flow cell. (g) Chronopotentiometry stability tests of NiFe LDH (+)||NW_1M_1R (−) at 1 A cm^{-2} and room temperature.

To reveal the effect of each component on the performance enhancement, we first employed density functional theory (DFT) to gain insights into the H* absorption/desorption trend. As shown in Fig. S30,† the ΔG_H of $Ni_{17}W_3$, WO_3, and MoO_3 is −0.60, 1.57, and 0.86 eV, respectively. Thus, the NW_1M_1R constructed $Ni_{17}W_3$ with a negative value and WO_3/MoO_3 with a positive value, indicating the potential hydrogen spillover process between the metal and metal oxide interface.[34,35] Then, the *in situ* Raman technique was utilized to monitor the phase evolution during the HER process. For the NWP sample, it is clear that the full width at half maximum (FWHM) of the O–W–O vibrational peak located at 325 cm^{-1} increases as the reaction proceeds, indicating a decrease in the crystallinity of WO_x (Fig. 3a).[36] Similarly, the characteristic peaks of W–O–W located at 820 and 843 cm^{-1} decreased when the negative voltage was applied.[37] The spontaneous disappearance in an alkaline environment contributes to surface reconstruction. Importantly, a new Raman signal appeared at 1055 cm^{-1} when

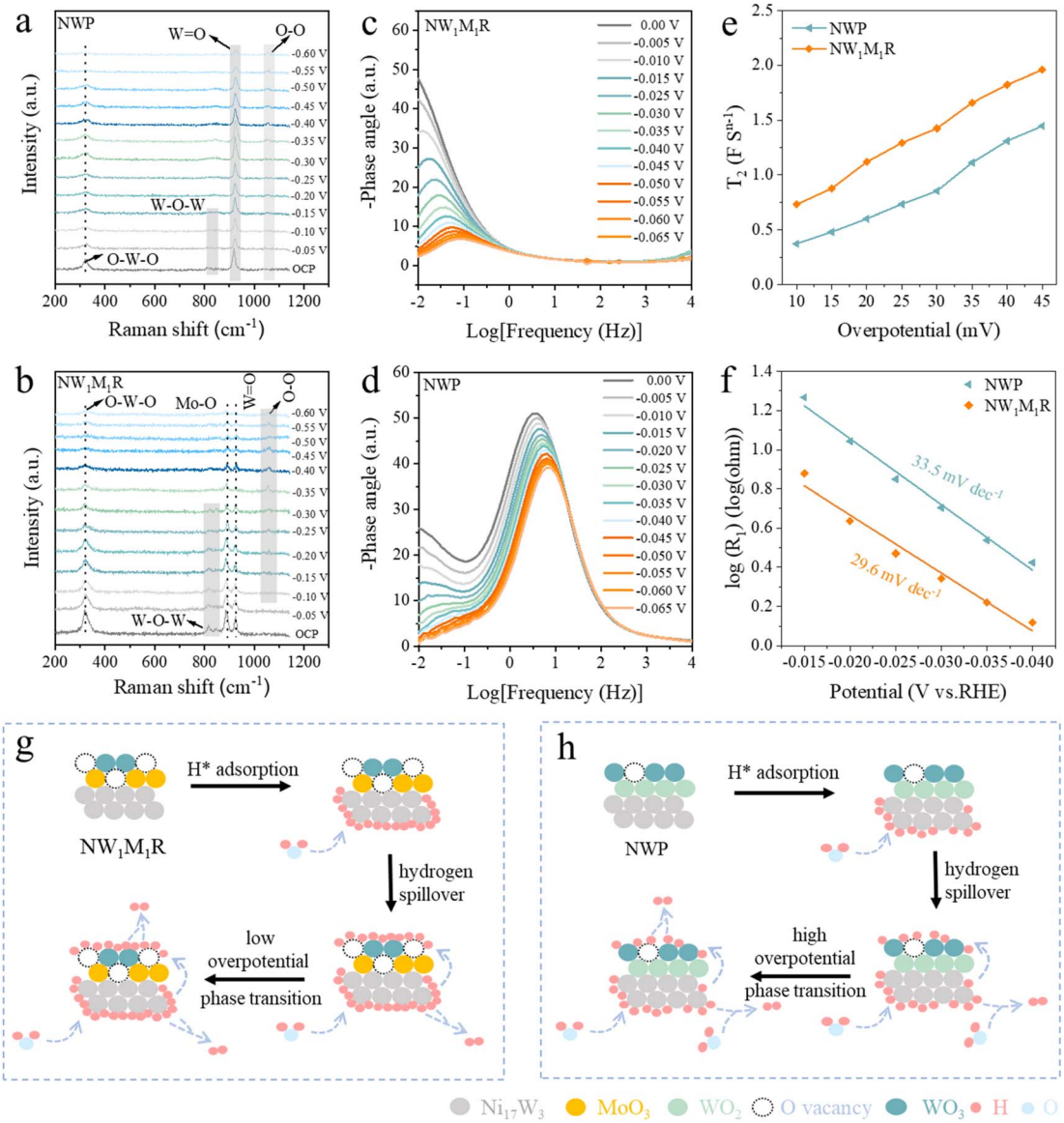

Fig. 3 (a and b) *In situ* Raman spectroscopy of NW_1M_1R and NWP. (c and d) *In situ* Bode phase plots of NW_1M_1R and NWP. (e) Plots of T_2 *vs.* η of NW_1M_1R and NWP. (f) Plots of log(R_1) *vs.* η of NW_1M_1R and NWP. Schematic illustration of the HER processes occurring on (g) NW_1M_1R and (h) NWP.

the voltage reaches −0.35 V,[38] which belongs to the metal oxide hydration vibration. In this way, metal oxide combines with water to form metal hydroxides, which further transform into hydrogen bronze with the assistance of electrons (eqn (1) and (2)). It should be noted that the hydrogen atoms in hydrogen bronze will dissociate into highly mobile protons and electrons. The protons are localized near the O^{2-} in the lattice, leading to hydroxide character, whereas the electrons localize on the metal d-orbitals, reducing the M^{6+} to M^{5+}. More importantly, the saturated concentration of protons will result in H_2 generation on the metal oxide surface (eqn (3)).

$$M^{VI}O_3 + H_2O \leftrightarrow M(OH)_x \quad (1)$$

$$M(OH)_x + H_2O + e^- \leftrightarrow H_yM^{V}M^{VI}O_{3-z} \quad (2)$$

$$H_yM^{V}M^{VI}O_{3-z} \leftrightarrow y/2H_2\uparrow + M^{VI}O_3 + e^- \quad (3)$$

For the NW_1M_1P sample, the characteristic peak of Mo–O stretching vibration appears at 887 cm^{-1} (Fig. 3b).[37] Meanwhile, the location of the characteristic peak of W=O shows a slight redshift, indicating that MoO_3 induces a change in the lattice stress–strain behavior.[39] Unlike the NWP sample, the W–O–W signal located at 820 and 843 cm^{-1} consistently has distinct characteristic peaks in the low voltage range (<−0.3 V), suggesting a stronger interaction between MoO_3 and WO_3, which is in agreement with the XPS results. Interestingly, the characteristic peaks of metal oxide hydration appear at a low voltage of −0.2 V, completing the phase transition from the metal oxide to the real active phase hydrogen bronze more quickly. The lower

activation potential of the NW_1M_1R electrocatalyst is supposed to be due to the fact that the high oxygen vacancies concentration is beneficial for the hydrogen insertion/extraction process.

In addition, due to the different HER kinetics based on the Tafel slope analysis, the *in situ* EIS technique was used to characterize the detailed mass/charge transfer kinetic behavior. Both samples were subjected to EIS analysis at different voltages (Fig. 3c and d). Bode plots can be divided into two regions, high-frequency and low-frequency, and the signals in each of these regions can be used to analyze the conductivity of the catalysts at the inner layer and the interface as well as the charge transfer between the catalysts and the electrolyte.[40] It is clear that the kinetics of NW_1M_1R and NWP are significantly different. NW_1M_1R has characteristic peaks only at low frequencies, indicating that the kinetic process is restricted to the charge/mass transfer process at the electrode/electrolyte interface.[41] Meanwhile, the almost negligible inner-layer/interface resistance can be attributed to the unique morphology and the SMSI effect. However, for NWP, the lower phase angle in the low-frequency area and the higher phase angle in the high-frequency area demonstrated that the kinetic process is mainly controlled by the inner layer/interface charge transfer resistance.[33] Then, the double-parallel equivalent circuit model is established based on the recorded Nyquist plots (Fig. S31 and S32†). The time constants of CPE_1 and R_1 can represent the hydrogen adsorption behavior, while CPE_2 and R_2 are related to the mass/charge transfer kinetics (Tables S2 and S3†).[14] Firstly, the lower resistance (R_1) of NW_1M_1R across the entire voltage range suggests efficient mass/charge transfer kinetics, in line with Tafel slope analysis. Then, the detailed H* adsorption/desorption behavior was further investigated. The H* adsorption charge can be represented by integrating the CPE_2-T with the overpotential (Fig. 3e). The larger area of NW_1M_1R than that of NWP indicates that NW_1M_1R adsorbs a larger amount of H*, and the higher H* coverage on the surface is conducive to the Volmer–Tafel process. In addition, the H* adsorption behavior of these two samples exhibits the potential-dependent increase as soon as the cathodic potential is applied, indicating that the hydrogen spillover phenomenon occurs at the interface; only the transfer efficiency from metal to support is different. Then, the desorption process of H* is investigated by analyzing the EIS-derived Tafel slope (Fig. 3f). The smaller slope proves that NW_1M_1R has a larger H* desorption charge, demonstrating that NW_1M_1R simultaneously has faster hydrogen desorption kinetics. In conclusion, compared to NWP, the kinetics of NW_1M_1R are limited only by the H* charging/mass transfer process and exhibit superior H* adsorption/desorption kinetics.

$$Ni_{17}W_3 + H_2O + e^- \leftrightarrow Ni_{17}W_3\text{–}H^* + OH^- \quad (4)$$

$$Ni_{17}W_3\text{–}H^* + Ni_{17}W_3\text{–}H^* + e^- \leftrightarrow Ni_{17}W_3 + H_2 \quad (5)$$

$$Ni_{17}W_3\text{–}H^* + MO_3 \leftrightarrow Ni_{17}W_3 + H_yM^{V}M^{VI}O_{3-z} \quad (6)$$

$$Ni_{17}W_3\text{–}H^* + H_2O + e^- \leftrightarrow Ni_{17}W_3 + H_2\uparrow + OH^- \quad (7)$$

Based on the analysis results, the HER process is detailed below. For the NM_1W_1R sample, the obvious hydrogen spillover occurs at the metal/metal oxide interface. First, the adjacent H* combine with each other on the metal surface to produce H_2 (eqn (4) and (5)). Then, due to the abundant oxygen vacancies of metal oxide support, the H* insertion/extraction proceeds easily in the metal oxide, resulting in a faster H* transfer from the metal to the metal oxide, leading to the metal oxide support surface, also producing significant amounts of hydrogen (eqn (3) and (6)). After increasing cathodic potential, the hydration capacity of metal oxides increased significantly, further promoting the phase transition process from metal oxides to hydrogen bronzes (eqn (2) and (3)). Thus, in turn, the whole H* adsorption, transfer, and desorption kinetic increased on the catalyst surface and interface, resulting in a superior HER performance. However, in the case of NMP, the lower H* coverage on the surface suggests that the transfer of H* from the metal to the metal oxide support is inefficient. The H_2 is produced primarily from the combination of H* on the surface and H_2O in the electrolyte, resulting in sluggish H* adsorption/desorption kinetics (eqn (4) and (7)). Meanwhile, the noticeable hydration of the metal oxide support requires a larger potential drive, and the kinetic behaviors of both hydrogen spillover and hydrogenation are relatively slow, resulting in unsatisfactory catalytic activity (Fig. 3g and h).

In order to verify whether the hydrogen spillover and metal oxide hydrogenation work at a wider pH range, the electrochemical performance of NM_1W_1R is investigated in 0.5 M H_2SO_4 (pH = 0.21) and 1.0 M PBS (pH = 7.2) electrolyte, respectively. Surprisingly, the same trend was observed under acidic and neutral conditions as under alkaline conditions. As shown in Fig. 4a and b, NW_1M_1R has the best HER performance

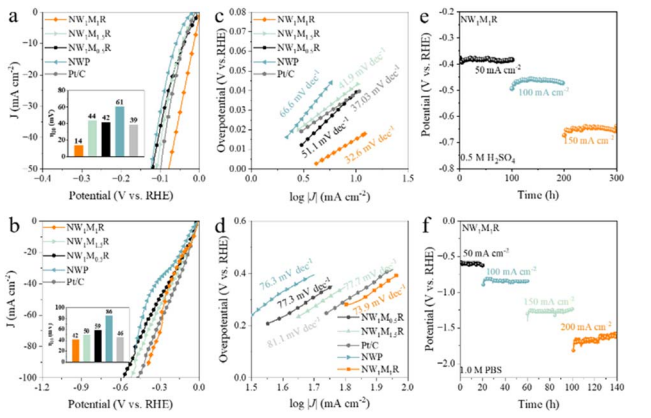

Fig. 4 (a) LSV curves of NW_1M_1R, $NW_1M_{1.5}R$, $NW_1M_{0.5}R$, NWP, and Pt/C (inset: overpotentials at 10 mA cm^{-2} for these electrocatalysts) in 0.5 M H_2SO_4. (b) LSV curves of NW_1M_1R, $NW_1M_{1.5}R$, $NW_1M_{0.5}R$, NWP, and Pt/C (inset: overpotentials at 10 mA cm^{-2} for these electrocatalysts) in 1.0 M PBS. (c) Tafel slope of different electrodes in 0.5 M H_2SO_4. (d) Tafel slope of different electrodes in 1.0 M PBS. (e) Multistep chronopotentiometry curves of NW_1M_1R at 50, 100, and 150 mA cm^{-2} for 300 h in 0.5 M H_2SO_4 (without *iR* correction). (f) Multistep chronopotentiometry curves of NW_1M_1R at 50, 100, 150, and 200 mA cm^{-2} for 140 h in 1.0 M PBS (without *iR* correction).

(14 mV in 0.5 M H_2SO_4 and 42 mV in 1.0 M PBS) compared to NWP (61 mV in 0.5 M H_2SO_4 and 86 mV in 1.0 M PBS), $NW_1M_{1.5}R$ (44 mV in 0.5 M H_2SO_4 and 50 mV in 1.0 M PBS), $NW_1M_{0.5}R$ (42 mV in 0.5 M H_2SO_4 and 59 mV in 1.0 M PBS) and Pt/C (39 mV in 0.5 M H_2SO_4 and 46 mV in 1.0 M PBS). The Tafel slope corresponding to NW_1M_1R (32.6 mV dec^{-1} in 0.5 M H_2SO_4 and 73.9 mV dec^{-1} in 1.0 M PBS) is similarly lower than that of NWP (66.6 mV dec^{-1} in 0.5 M H_2SO_4 and 76.3 mV dec^{-1} in 1.0 M PBS), $NW_1M_{1.5}R$ (41.9 dec^{-1} in 0.5 M H_2SO_4 and 77.7 mV dec^{-1} in 1.0 M PBS), $NW_1M_{0.5}R$ (51.1 mV dec^{-1} in 0.5 M H_2SO_4 and 77.3 mV dec^{-1} in 1.0 M PBS) and Pt/C (37.03 mV dec^{-1} in 0.5 M H_2SO_4 and 81.1 mV dec^{-1} in 1.0 M PBS) (Fig. 4c and d). The long-term HER performance of NW_1M_1R at different current densities and in different electrolytes (300 h in 0.5 M H_2SO_4 and 140 h in 1.0 M PBS) shows no significant upward trend in voltage (Fig. 4d and e). These results demonstrate that NW_1M_1R could serve as a superior pH-universal electrocatalyst for HER.

Conclusions

In summary, we designed and prepared the $Ni_{17}W_3/MoO_{3-x}/WO_{3-x}$ catalyst for HER reaction at all pH values. This catalyst prepared *via* the *in situ* confinement method provided a large specific surface area, ensuring the total exposure of active sites to the electrolyte. Importantly, the electrochemical performance can be regulated by adjusting the metal oxide support's oxygen vacancy concentration. Combined with DFT, *in situ* Raman, and *in situ* EIS results, we prove that the abundant oxygen vacancies in the WO_{3-x}/MoO_{3-x} support is beneficial for the improvement of hydrogen intermediate insertion/extraction kinetic and hydration capacity, resulting in a faster hydrogen intermediate absorption/transfer/desorption kinetics on the catalyst surface and interface, thus achieving a superior HER performance. As a result, the prepared catalysts exhibited overpotentials of only 16, 42, and 14 mV at current densities of 10 mA cm^{-2} in the alkaline, neutral, and acid conditions, respectively. Our work not only shows the potential practical application of the fabricated electrocatalyst but also provides a new insight into the electrocatalyst design of metal/metal oxide.

Conflicts of interest

There are no conflicts to declare.

Acknowledgements

This work is financially supported by the Shanghai Sailing Program (23YF1455000) and the City University of Hong Kong (Project 7020088 and 9229138).

References

1 D. Li, A. R. Motz, C. Bae, C. Fujimoto, G. Yang, F.-Y. Zhang, K. E. Ayers and Y. S. Kim, *Energy Environ. Sci.*, 2021, **14**, 3393–3419.
2 M. Chen, N. Kitiphatpiboon, C. Feng, A. Abudula, Y. Ma and G. Guan, *eScience*, 2023, **3**, 100111–100127.
3 L. Dong, G.-R. Chang, Y. Feng, X.-Z. Yao and X.-Y. Yu, *Rare Met.*, 2022, **41**, 1583–1594.
4 Y. S. Park, F. Liu, D. Diercks, D. Braaten, B. Liu and C. Duan, *Appl. Catal., B*, 2022, **318**, 121824–121833.
5 Q. Qian, X. He, Z. Li, Y. Chen, Y. Feng, M. Cheng, H. Zhang, W. Wang, C. Xiao, G. Zhang and Y. Xie, *Adv. Mater.*, 2023, **35**, 2300935–2300948.
6 Y. Shi, Z. R. Ma, Y. Y. Xiao, Y. C. Yin, W. M. Huang, Z. C. Huang, Y. Z. Zheng, F. Y. Mu, R. Huang, G. Y. Shi, Y. Y. Sun, X. H. Xia and W. Chen, *Nat. Commun.*, 2021, **12**, 3021–3032.
7 Y. Li, W. Wang, M. Cheng, Y. Feng, X. Han, Q. Qian, Y. Zhu and G. Zhang, *Adv. Mater.*, 2023, **35**, 2206351–2206361.
8 F. Li, G. F. Han, H. J. Noh, J. P. Jeon, I. Ahmad, S. S. Chen, C. Yang, Y. F. Bu, Z. P. Fu, Y. L. Lu and J. B. Baek, *Nat. Commun.*, 2019, **10**, 4060–4067.
9 Y. Feng, X. He, M. Cheng, Y. Zhu, W. Wang, Y. Zhang, H. Zhang and G. Zhang, *Small*, 2023, **19**, 2301986–2301995.
10 X. Wang, X. Yang, G. Pei, J. Yang, J. Liu, F. Zhao, F. Jin, W. Jiang, H. Ben and L. Zhang, *Carbon Energy*, 2023, e391.
11 Z. Z. Jiang, Z. B. Wang, Y. Y. Chu, D. M. Gu and G. P. Yin, *Energy Environ. Sci.*, 2011, **4**, 2558–2566.
12 G. N. Vayssilov, Y. Lykhach, A. Migani, T. Staudt, G. P. Petrova, N. Tsud, T. Skála, A. Bruix, F. Illas, K. C. Prince, V. Matolín, K. M. Neyman and J. Libuda, *Nat. Mater.*, 2011, **10**, 310–315.
13 W. Zhang, B. Huang, K. Wang, W. Yang, F. Lv, N. Li, Y. Chao, P. Zhou, Y. Yang, Y. Li, J. Zhou, W. Zhang, Y. Du, D. Su and S. Guo, *Adv. Energy Mater.*, 2021, **11**, 2003192–2003199.
14 J. Li, J. Hu, M. Zhang, W. Gou, S. Zhang, Z. Chen, Y. Qu and Y. Ma, *Nat. Commun.*, 2021, **12**, 3502–3514.
15 J. Li, H.-X. Liu, W. Gou, M. Zhang, Z. Xia, S. Zhang, C.-R. Chang, Y. Ma and Y. Qu, *Energy Environ. Sci.*, 2019, **12**, 2298–2304.
16 J. Park, S. Lee, H.-E. Kim, A. Cho, S. Kim, Y. Ye, J. W. Han, H. Lee, J. H. Jang and J. Lee, *Angew. Chem., Int. Ed.*, 2019, **58**, 16038–16042.
17 C. Jian, Q. Cai, W. Hong, J. Li and W. Liu, *Int. J. Hydrogen Energy*, 2017, **42**, 17030–17037.
18 C. Han, D. Wang, Q. Li, Z. Xing and X. Yang, *ACS Appl. Energy Mater.*, 2019, **2**, 2409–2413.
19 J. Liu, G. Qian, T. Yu, J. Chen, C. Zhu, Y. Li, J. He, L. Luo and S. Yin, *Chem. Eng. J.*, 2022, **431**, 134247–134256.
20 H.-S. Kim, J. B. Cook, H. Lin, J. S. Ko, S. H. Tolbert, V. Ozolins and B. Dunn, *Nat. Mater.*, 2017, **16**, 454–463.
21 J. Zhang, T. Wang, P. Liu, Z. Liao, S. Liu, X. Zhuang, M. Chen, E. Zschech and X. Feng, *Nat. Commun.*, 2017, **8**, 15437–15445.
22 Y. Tang, L. Dong, H. B. Wu and X.-Y. Yu, *J. Mater. Chem. A*, 2021, **9**, 1456–1462.
23 W. Xu, B. Wang, X. Ni, H. Liu, W. Wang, L. Zhang, H. Zhang, Z. Peng and Z. Liu, *ACS Appl. Mater. Interfaces*, 2021, **13**, 13838–13847.
24 T. Wang, X. Cao and L. Jiao, *eScience*, 2021, **1**, 69–74.
25 Q. Qi, D. Shao, Y. Zhou, Q. Wang and X.-Y. Yu, *J. Mater. Chem. A*, 2023, **11**, 15663–15669.

26 O. Karslioglu, X. Song, H. Kuhlenbeck and H.-J. Freund, *Top. Catal.*, 2013, **56**, 1389–1403.
27 F. Nacimiento, M. Cabello, R. Alcantara, C. Perez-Vicente, P. Lavela and J. L. Tirado, *J. Electrochem. Soc.*, 2018, **165**, A2994–A2999.
28 Z. Wang, X. Mao, P. Chen, M. Xiao, S. A. Monny, S. Wang, M. Konarova, A. Du and L. Wang, *Angew. Chem., Int. Ed.*, 2019, **58**, 1030–1034.
29 L. Xu, Q. Jiang, Z. Xiao, X. Li, J. Huo, S. Wang and L. Dai, *Angew. Chem., Int. Ed.*, 2016, **55**, 5277–5281.
30 X. Hu, J. Wang, J. Wang, Y. Deng, H. Zhang, T. Xu and W. Wang, *Appl. Catal., B*, 2022, **318**, 121879–121894.
31 Y. Yang, Z. Wang, P. Yan and X.-Y. Yu, *Appl. Phys. Lett.*, 2023, **123**, 033903–033910.
32 G. Yang, Y. Jiao, H. Yan, Y. Xie, C. Tian, A. Wu, Y. Wang and H. Fu, *Nat. Commun.*, 2022, **13**, 3125–3137.
33 C. Xie, W. Chen, S. Du, D. Yan, Y. Zhang, J. Chen, B. Liu and S. Wang, *Nano Energy*, 2020, **71**, 104653–104661.
34 R. Prins, *Chem. Rev.*, 2012, **112**, 2714–2738.
35 W. Karim, C. Spreafico, A. Kleibert, J. Gobrecht, J. VandeVondele, Y. Ekinci and J. A. van Bokhoven, *Nature*, 2017, **541**, 68–71.
36 G. Poirier, Y. Messaddeq, S. J. L. Ribeiro and M. Poulain, *J. Solid State Chem.*, 2005, **178**, 1533–1538.
37 E. I. Ross-Medgaarden and I. E. Wachs, *J. Phys. Chem. C*, 2007, **111**, 15089–15099.
38 C. R. Santiago-Ramirez, J. Vera-Iturriaga, P. del Angel, A. Manzo-Robledo, M. L. Hernandez-Pichardo and J. Soto-Hernandez, *Appl. Catal., B*, 2021, **282**, 119545–119558.
39 J. Dai, Y. Zhu, Y. Chen, X. Wen, M. Long, X. Wu, Z. Hu, D. Guan, X. Wang, C. Zhou, Q. Lin, Y. Sun, S.-C. Weng, H. Wang, W. Zhou and Z. Shao, *Nat. Commun.*, 2022, **13**, 1189–1199.
40 J. Huang, H. Sheng, R. D. Ross, J. Han, X. Wang, B. Song and S. Jin, *Nat. Commun.*, 2021, **12**, 3036–3047.
41 Y.-Y. Chen, Y. Zhang, X. Zhang, T. Tang, H. Luo, S. Niu, Z.-H. Dai, L.-J. Wan and J.-S. Hu, *Adv. Mater.*, 2017, **29**, 1703311–1703318.